Evaluation of the probability density of orientations for inhomogeneities by computed tomography and its application to the calculation of the effective properties of a fiber reinforced concrete.

Tatiana Mishurova[1], Natalia Rachmatullin[1], Patrick Fontana[1], Tyler S. Oesch[1], Giovanni Bruno[1], Enrico Radi[2], Igor Sevostianov[3*]

[1] Federal Institute of Materials Research and Testing - BAM, Unter den Eichen 87, 12205 Berlin, Germany.

[2] Dipartimento di Scienze e Metodi dell'Ingegneria, Università di Modena e Reggio Emilia, Via Amendola, 2 - 42122 Reggio Emilia, Italy.

[3] Department of Mechanical and Aerospace Engineering, New Mexico State University, Las Cruces, NM 88001, USA. * Author for correspondence: igor@nmsu.edu

Abstract. The paper focuses on the experimental evaluation of one of the key microstructural parameters of a short fiber reinforced composite –orientation distribution of fibers. It is shown that computed tomography produce results suitable for reconstruction of the orientation distribution function. This function is used for calculation of the effective elastic properties of polymer fiber reinforced concrete. We derive explicit formulas for overall elastic moduli accounting for orientation distribution in the frameworks of non-interaction approximation, Mori-Tanaka-Benveniste scheme, and Maxwell scheme. The approach illustrated can be applied to any kind of composite material..

Keywords: computed tomography, orientation distribution, effective properties, fiber reinforced composite.

ha formattato: Italiano (Italia)

ha formattato: Italiano (Italia)

ha formattato: Italiano (Italia)

1. Introduction.

The present paper focuses on the integration of computed tomography data into micromechanical homogenization techniques to account for orientation distribution of non-spherical inhomogeneities in heterogeneous materials. In short fiber reinforced composites the fibers are usually neither perfectly parallel, nor perfectly randomly oriented, but have certain orientation distribution (Figure 1), which belongs to the major factors affecting the overall properties (Kachanov and Sevostianov, 2005). However, non-spherical inhomogeneities in composites have been considered as perfectly aligned till the beginning of 1980s. To the best of our knowledge, random orientation of fibers has been first considered by Chou and Nomura (1980-1981) and Takao et al (1982), who applied average induced strain approach to composites with 3-D randomly oriented short fibers. The averaging procedure was later used by Benveniste (1987) and Chen et al (1992) in the Mori-Tanaka scheme. Tandon and Weng (1986) considered two cases of random distribution of fibers - in space (overall isotropy) and in-plane (overall transverse isotropy). General case of the orientation distribution of short fibers has been first discussed by Ferrari and Johnson (1989) who presented a theoretical scheme in which the fiber orientation distribution was allowed to be arbitrarily specified. The authors first introduced an orientation distribution function (ODF) defined over the full Euler space. This approach was implemented into the Mori-Tanaka scheme by Ferrari (1991) and Marzari and Ferrari (1992).

In the successive years many specific ODF have been discussed in literature. Lu and Liaw (1995) considered fiber reinforced composite and assumed independence of the orientation distribution of fibers with respect to different Euler angles ϕ, θ, φ, so that $P(\phi, \theta, \varphi) = P(\phi)P(\theta)P(\varphi)$ ($0 \le \phi, \theta, \varphi \le \pi$). They used a combination of Gaussian and trigonometric distributions

$$P(\phi) = \frac{2 + cos(2\phi)}{2\pi};\ P(\theta) = \sqrt{\frac{2}{\pi}}\, exp\left(\frac{-(\theta - \pi/2)^2}{2}\right);\ P(\varphi) = \sqrt{\frac{2}{\pi}}\, exp\left(\frac{-(\varphi - \pi/2)^2}{2}\right) \quad (1.1)$$

which fit the distribution obtained by quantitative image analysis of SEM pictures. Applicability of this function to non-random orientation distribution is, however, unclear.

Chen and Wang (1996) calculated the effective thermal conductivity of a transversely isotropic composite containing misoriented inhomogeneities. The orientation distribution was described by

$$P(\theta) = 1 - exp(\lambda\theta) \tag{1.2}$$

where the zero value of the scatter parameter λ corresponds to random distribution of the inhomogeneities and high values indicate a highly oriented material.

Dunn et al (1996) considered SiC/Al short fiber reinforced composites and evaluated ODF using neutron-diffraction techniques (suitable for monocrystalline fibers). They expanded the orientation-distribution function in a series of generalized spherical harmonics and suggested to use the eighth-order transformation tensor relating a fourth-order tensor in the local and global coordinate systems. This approach was later used by Dunn and Ledbetter (1997, 2000) for the calculation of elastic-plastic and thermo-elastic properties of short-fiber reinforced composites and by Li (2000) for the calculation of piezoelectric properties.

A detailed analysis of the effect of the inclusion orientation distribution on the effective thermomechanical properties has been done by Pettermann et al (1997) who used the Mori-Tanaka scheme and assumed exponential ODF

$$P(\theta) = exp\left(-\theta^2 / 2\lambda^2\right) \tag{1.3}$$

This can be regarded as a truncated axisymmetric Gaussian distribution. The authors calculated overall Young's moduli, shear moduli and coefficients of thermal expansion, as well as the onset of yielding of the matrix phase under thermal and mechanical loading conditions. Duschlbauer et al (2003) used this approach for calculation of the effective thermal properties of composites.

Fu and Lauke (1998) used a two-parameter ODF

$$P(\theta) = \frac{(sin\theta)^{2p-1}(cos\theta)^{2q-1}}{\int_{\theta_{min}}^{\theta_{max}} (sin\theta)^{2p-1}(cos\theta)^{2q-1} d\theta}; \; 0 \le \theta_{min} \le \theta \le \theta_{max} \le \pi/2 \tag{1.4}$$

where p and q are the shape parameters which can be used to determine the shape of the distribution curves. A similar model (with one parameter) was used by Zhupanska (2013) to calculate mechanical properties of buckypaper nanocomposite. Turner et al (1999) used a Gaussian distribution for each Euler angle, assuming those distributions as statistically independent, and calculated effective mechanical properties and phase average stresses in SiC/Al composites. Similar approaches have been adopted by Fernandez et al.(2005) and Bruno and Fernandez (2008). Sevostianov and Kachanov (2000) considering transversely isotropic orientation distribution of cracks suggested to use ODF in the form

$$P_\lambda(\varphi) = \frac{1}{2\pi}\left[\left(\lambda^2+1\right)e^{-\lambda\varphi} + \lambda e^{-\lambda\pi/2}\right] \quad (1.5)$$

This function was used later by Sevostianov *et al* (2016) to calculate viscoelastic properties of short fiber reinforced composites.

Kachanov et al (1994) showed that the form of the ODF does not noticeably affect the overall elastic and conductive properties of a composite. Thus the specific choice is mostly dictated by computational convenience. A more important issue is related to the experimental evaluation of the ODF and the incorporation of experimental data into analytical formulas. Certain progress in this direction has been obtained during the last decade.

Perez et al (2008) determined the ODF in aligned single wall nanotube polymer nanocomposites using polarized Raman spectroscopy. Blanco (2013) analyzed various destructive and non-destructive methods for fiber orientation determination. Most of them are based on electrical resistivity and inductivity of fibers (see, for example, Lataste, 2008), which are applicable for metallic fibers only.

Another possibility to evaluate fiber orientation distribution is analysis of 2D images obtained by different methods. Considering extraction fiber orientation information from radiographs, Fourier image transform was proposed in Redon et al. (1998, 1999). Lee et al. (2009) suggested to use digital image analysis. This technique was practically implemented by Kanga et al. (2011, 2012). One of the most widely used 2-D methods for evaluation of fiber orientation is microscopy that evaluate ODF from the analysis of cross sections (Zhu et al., 1997, Tsuda, 2014). Clarke and Eberhardt (1999, 2001) showed that fiber orientation analysis can be performed by using confocal microscopy. However, microscopy methods are very time-consuming (Bay et al., 1992), and connection between 3-D microstructure and its 2-D images is still an open question. Bernasconi et al. (2012) and Liu et al (2013) performed comparison between 2D optical methods and computed tomography (CT). Their results show that CT measurements have higher accuracy in evaluation of fiber orientation as compared to 2D image analysis. Suuronen el al. (2013) used CT measurements to study orientation distribution probability density in steel fiber reinforced concrete. Pujadas et al. (2014 a, b) discussed the link between the mechanical properties of fiber reinforced concrete and the fiber orientation. In particularly, they proved the efficiency of CT technique to evaluate the fiber orientation, but they

did not perform orientation distribution probability density analysis, and consequently did not insert ODF into their model.

In the present paper, we use CT reconstructions to evaluate ODF in the form (1.5) and integrate the result into explicit expressions for effective elastic moduli of a polymer fiber reinforced concrete. The approach is based on the concept of property contribution tensors and is illustrated by using different homogenization schemes. We finally compare the calculations with experimental data of Young's modulus obtained by three-point bending tests.

2. Calculation of the effective elastic properties of a composite with non-randomly oriented inhomogeneities.

2.1.Background results – property contribution tensors.

Property contribution tensors are used in the context of homogenization problems to describe contribution of a single inhomogeneity to the property of interest – elasticity, thermal or electrical conductivity, diffusion coefficient, etc. In the context of the effective elastic properties, one can use the compliance contribution tensor of an inhomogeneity $\boldsymbol{H}$, which gives the extra strain produced by the introduction of the inhomogeneity in the otherwise uniform stress field, or the stiffness contribution tensor $\boldsymbol{N}$, which gives the extra stress due to the inhomogeneity when it is placed into the otherwise uniform strain field.

Compliance contribution tensors have been first introduced in the context of pores and cracks by Horii and Nemat-Nasser (1983) (see also detailed discussion in the book of Nemat-Nasser and Hori, 1993). For the general case of elastic inhomogeneities, these tensors were given for ellipsoidal shapes by Sevostianov and Kachanov (1999, 2002). For the reader's convenience, we provide below a brief description of the property contribution tensors.

We first consider a homogeneous *elastic* material (matrix), with compliance and stiffness tensors $\boldsymbol{S}^0$ and $\boldsymbol{C}^0$, assumed to be isotropic. The matrix contains an inhomogeneity, of volume $V^{(1)}$, of a different elastic material with compliance and stiffness tensors $\boldsymbol{S}^1$ and $\boldsymbol{C}^1$. The contribution of the inhomogeneity to the overall strain per representative volume V (the extra strain, as compared to the homogeneous matrix) is given by

$$\Delta\boldsymbol{\varepsilon} = \frac{V^{(1)}}{V}\boldsymbol{H} : \boldsymbol{\sigma}^{\infty} \qquad (2.1)$$

where $\boldsymbol{\sigma}^{\infty}$ is the "remotely applied" stress field, that, in absence of the inhomogeneity, would have been uniform within its site ("homogeneous boundary conditions", Hashin, 1983); a colon denotes contraction over two indices (Note that Eq.(2.1) represents the definition of the fourth-rank tensor $\boldsymbol{H}$ – the compliance contribution tensor of the inhomogeneity). In the case of multiple inhomogeneities, the extra compliance due to their presence is given by

$$\Delta \boldsymbol{S} = \frac{1}{V}\sum V^{(k)*}\boldsymbol{H}^{(k)} \tag{2.2}$$

Alternatively, one can consider the extra average (over V) stress $\Delta\boldsymbol{\sigma}$ due to an inhomogeneity under uniform displacement boundary conditions (displacements on ∂V have the form $\boldsymbol{u}|_{\partial V} = \boldsymbol{\varepsilon}^0 \cdot \boldsymbol{n}$ where $\boldsymbol{\varepsilon}^0$ is a constant tensor). This defines the *stiffness contribution tensor* $\boldsymbol{N}$ of an inhomogeneity:

$$\Delta\boldsymbol{\sigma} = \frac{V^{(1)}}{V}\boldsymbol{N} : \boldsymbol{\varepsilon}^0, \tag{2.3}$$

In the case of multiple inhomogeneities, the extra stiffness due to inhomogeneities is given by

$$\Delta \boldsymbol{C} = \frac{1}{V}\sum V^{(k)*}\boldsymbol{N}^{(k)} \tag{2.4}$$

The $\boldsymbol{H}$- and $\boldsymbol{N}$-tensors are determined by the shape of the inhomogeneity and are independent of its size; they also depend on the elastic constants of the matrix and of the inhomogeneity.

For the ellipsoidal inhomogeneity, the fourth-order tensors $\boldsymbol{H}$ and $\boldsymbol{N}$ can be expressed in terms of elastic contrast (i.e., the difference between stiffness $\boldsymbol{C}$ or compliance $\boldsymbol{S}$ of matrix and inhomogeneity), and of the fourth-order Hill's tensors $\boldsymbol{P}$ and $\boldsymbol{Q}$, which describe the effects of shape of the inhomogeneity:

$$\boldsymbol{H} = \left[\left(\boldsymbol{S}^1 - \boldsymbol{S}^0\right)^{-1} + \boldsymbol{Q}\right]^{-1}, \qquad \boldsymbol{N} = \left[\left(\boldsymbol{C}^1 - \boldsymbol{C}^0\right)^{-1} + \boldsymbol{P}\right]^{-1} \tag{2.5}$$

Note that the effects of elastic contrast and shape of the inhomogeneity can be separated for ellipsoidal shapes. The fourth-order Hill's (1965) tensor $\boldsymbol{P}$ is the integral over the volume of the inhomogeneity from the second gradient of Green's tensor and tensor $\boldsymbol{Q}$ is related to $\boldsymbol{P}$ as follows (Walpole, 1966):

$$Q_{ijkl} = C^0_{ijmn}\left(J_{mnkl} - P_{mnrs}C^0_{rskl}\right) \tag{2.6}$$

Here, $J_{ijkl} = \left(\delta_{ik}\delta_{lj} + \delta_{il}\delta_{kj}\right)/2$ and the inverse of symmetric (with respect to $i \leftrightarrow j$ and $k \leftrightarrow l$) fourth-order tensor X^{-1}_{ijkl} is defined by $X^{-1}_{ijmn}X_{mnkl} = X_{ijmn}X^{-1}_{mnkl} = J_{ijkl}$.

For a spheroidal inhomogeneity (with semi-axes $a_3; a_1 = a_2$) embedded in an isotropic matrix, it is convenient to use representation of these tensors in terms of standard tensor basis $\boldsymbol{T}^{(1)},...,\boldsymbol{T}^{(6)}$ (see Appendix for detail):

$$\boldsymbol{P} = \sum_{k=1}^{6} p_k \boldsymbol{T}^{(k)} \;;\; \boldsymbol{Q} = \sum_{k=1}^{6} q_k \boldsymbol{T}^{(k)} \;;\; \boldsymbol{H} = \sum_{k=1}^{6} h_k \boldsymbol{T}^{(k)} \;;\; \boldsymbol{N} = \sum_{k=1}^{6} n_k \boldsymbol{T}^{(k)} \tag{2.7}$$

so that finding out these tensors reduces to the calculation of factors p_k, q_k, h_k and n_k. The relations for these coefficients are given in the Appendix.

<u>*Remark.*</u> Generally, $\boldsymbol{H}$- and $\boldsymbol{N}$-tensors in (2.2) and (2.4) have to reflect the interactions between the inhomogeneities. However, incorporating interactions into the micromechanical parameter amounts to solving the interaction problem, and hence it is not practical. Contributions of individual inhomogeneities are taken by treating them as *non-interacting* ones (in particular, mutual positions of inhomogeneities are not reflected) and then used in various approximate schemes that aim at accounting for interactions (effective media and effective field approaches)

2.2. Effective elastic stiffnesses.

If the interaction between inhomogeneities is neglected, the change in the elastic compliances (or stiffnesses) due to the inhomogeneities is calculated by (2.2) (or (2.4)). If the inhomogeneities in a composite have the same shape, size, and properties and their orientation is described by a known ODF, it is convenient to replace summation in $\sum V^{(k)*}\boldsymbol{H}^{(k)}$ and $\sum V^{(k)*}\boldsymbol{N}^{(k)}$ by averaging over the orientations, so that

$$\boldsymbol{S} = \boldsymbol{S}_0 + c\langle \boldsymbol{H} \rangle \;;\; \boldsymbol{C} = \boldsymbol{C}_0 + c\langle \boldsymbol{N} \rangle \tag{2.8}$$

where c is the volume fraction of the inhomogeneities.

Following Sevostianov and Kachanov (2000), we express the unit vector $\boldsymbol{m}$ along the *i*-th spheroid's symmetry axis in terms of two angles $0 \le \varphi \le \pi/2$ and $0 \le \theta \le 2\pi$ (Figure 2):

$$\boldsymbol{m}(\varphi,\theta) = \cos\theta \sin\varphi\, \boldsymbol{e_1} + \sin\theta \sin\varphi\, \boldsymbol{e}_2 + \cos\varphi\, \boldsymbol{e}_3 \tag{2.9}$$

and use statistics $P(\varphi,\theta)$ of fibers orientation - the probability density function defined on the upper semi-sphere of unit radius and subject to the normalization condition

$$\int_0^{2\pi}\int_0^{\pi/2} P(\varphi,\theta)\sin\varphi d\varphi d\theta = 1 \tag{2.10}$$

We assume that the orientation distributions of fibers with respect to angles θ and φ are independent so that $P(\varphi,\theta)=P(\varphi)P(\theta)$, and consider the distributions that are intermediate between the random and the parallel ones, by specifying the following probability density containing the scatter parameter ζ :

$$P_{\zeta_\varphi}(\varphi)=\left(\zeta_\varphi^2+1\right)e^{-\zeta_\varphi\varphi}+\zeta_\varphi e^{-\zeta_\varphi\pi/2} \quad ; \; P_{\zeta_\theta}(\theta)=\frac{\zeta_\theta}{2}\,e^{-\zeta_\theta\left|\theta-\pi\right|-\pi\left|\right.}+\frac{1}{2\pi}e^{-\zeta_\theta\pi} \tag{2.11}$$

Parameters ζ characterize the sharpness of the peak and the extent of the scatter; the extreme cases of the fully random and perfectly parallel fibers correspond to $\zeta=0$ and $\zeta\to\infty$ respectively. Note that the effective elastic moduli are relatively insensitive to the exact form of a function that has the above-mentioned features (Kachanov et al, 1994). Figure 3 shows dependencies of $P_\zeta(\varphi)$ on φ and $P_\zeta(\theta)$ on θ for several values of ζ. For the reader's convenience behavior of $P_\zeta(\varphi)\sin\varphi$ is also illustrated. Now, if parameter ζ is known, the following two tensors – averages over the orientation of fibers - can be evaluated:

$$A_{ij}=\left\langle m_i m_j\right\rangle \qquad\qquad B_{ijkl}=\left\langle m_i m_j m_k m_l\right\rangle \tag{2.12}$$

where components of the unit vector along a fiber in spherical coordinate system are given by (2.9). This operation is equivalent to averaging of basic tensors $\boldsymbol{T}^{(i)}$ given by (A.1) over orientation of vectors $\boldsymbol{m}^{(p)}$. In particular, if the orientation distribution with respect to θ is approximately random (parameter ζ_θ is sufficiently large),

$$\begin{aligned}&\left\langle \boldsymbol{mm}\right\rangle = g_1(\zeta)\boldsymbol{\theta}+g_2(\zeta)\boldsymbol{e_i e_i}\\ &\left\langle \boldsymbol{mmmm}\right\rangle = g_3(\zeta)\left(\boldsymbol{T}^{(1)}+\boldsymbol{T}^{(2)}\right)+g_4(\zeta)\left(\boldsymbol{T}^{(3)}+\boldsymbol{T}^{(4)}+\boldsymbol{T}^{(5)}\right)+g_5(\zeta)\boldsymbol{T}^{(6)}\end{aligned} \tag{2.13}$$

where $\theta_{ij}=\delta_{ij}-m_i m_j$ and

$$g_1(\zeta)=\frac{18-\zeta\left(\zeta^2+3\right)e^{-\zeta\pi/2}}{6\left(\zeta^2+9\right)}; \qquad g_2(\zeta)=\frac{3\left(\zeta^2+3\right)+\zeta\left(\zeta^2+3\right)e^{-\zeta\pi/2}}{3\left(\zeta^2+9\right)} \tag{2.14}$$

$$g_3(\zeta)=\frac{30}{\left(\zeta^2+9\right)\left(\zeta^2+25\right)}-\zeta e^{-\zeta\pi/2}\left[\frac{1\left(\zeta^4+30\zeta^2+149\right)}{4\left(\zeta^2+9\right)\left(\zeta^2+25\right)}-\frac{2}{15}\right]$$

$$g_4(\zeta)=\frac{3\zeta^2}{\left(\zeta^2+9\right)\left(\zeta^2+25\right)}+\zeta e^{-\zeta\pi/2}\left[\frac{\zeta^4+22\zeta^2+45}{8\left(\zeta^2+9\right)\left(\zeta^2+25\right)}\right]$$

$$g_5(\zeta)=\frac{\zeta^2\left(\zeta^2+7\right)}{\left(\zeta^2+9\right)\left(\zeta^2+25\right)}-\zeta e^{-\zeta\pi/2}\left[\frac{\zeta^4+10\zeta^2-15}{4\left(\zeta^2+9\right)\left(\zeta^2+25\right)}\right] \qquad (2.15)$$

and components of tensor basis $\boldsymbol{T}^{(i)}$ are given in the Appendix by (A.1). Functions $g_i(\zeta)$ are shown in Figure 4. Then the orientation average tensor

$$\langle \boldsymbol{H} \rangle = \sum_{k=1}^{6} h_k^* \boldsymbol{T}^{(k)} \qquad (2.16)$$

is transversely isotropic with the symmetry axis x_3 and is characterized by the following coefficients:

$$h_1^* = h_1 + g_1(\zeta)\left[h_3 + h_4 + \frac{1}{2}h_5\right] + g_3(\zeta)h_6; \qquad h_2^* = h_2 + g_1(\zeta)h_5 + g_3(\zeta)h_6;$$

$$h_3^* = g_2(\zeta)\left(h_3 + h_4\right) + g_4(\zeta)h_6; \quad h_4^* = h_3^*$$

$$h_5^* = g_2(\zeta)h_5 + g_4(\zeta)h_6; \; h_6^* = g_5(\zeta)h_6 \qquad (2.17)$$

where h_i are given by (A.15). Similar formulas can be written for tensor $\langle \boldsymbol{N} \rangle$.

In the isotropic case of the inhomogeneities randomly oriented in-space

$$\langle m_i m_j \rangle = \frac{1}{3}\delta_{ij}; \; \langle m_i m_j m_k m_l \rangle = \frac{1}{15}\left(\delta_{ij}\delta_{kl} + \delta_{ik}\delta_{jl} + \delta_{il}\delta_{jk}\right) \qquad (2.18)$$

So that

$$h_1^* = \frac{1}{30}\left(14h_1 + 2h_2 + 6h_3 + 6h_4 + h_5 + 4h_6\right); \; h_2^* = \frac{1}{30}\left(4h_1 + 12h_2 - 4h_3 - 4h_4 + 6h_5 + 4h_6\right)$$

$$h_3^* = h_4^* = \frac{1}{30}\left(12h_1 - 4h_2 + 8h_3 + 8h_4 - 2h_5 + 2h_6\right)$$

$$h_5^* = \frac{1}{30}\left(8h_1 + 24h_2 - 8h_3 - 8h_4 + 12h_5 + 8h_6\right);$$

$$h_6^* = \frac{1}{30}\left(16h_1 + 8h_2 + 4h_3 + 4h_4 + 4h_5 + 6h_6\right) \qquad (2.19)$$

In the transversely-isotropic case of the inhomogeneities randomly oriented in- plane

$$\langle m_i m_j \rangle = \frac{1}{2}\theta_{ij}. \quad \langle m_i m_j m_k m_l \rangle = \frac{1}{8}\left(\theta_{ij}\theta_{kl} + \theta_{ik}\theta_{jl} + \theta_{il}\theta_{jk}\right) = \frac{1}{4}\left(\boldsymbol{T}^{(1)} + \boldsymbol{T}^{(2)}\right) \tag{2.20}$$

and

$$h_1^* = \frac{1}{8}\left(2h_1 + h_2 + 6h_3 + 6h_4 + 2h_5 + 2h_6\right);\ h_2^* = \frac{1}{8}\left(2h_1 - 7h_2 - 2h_3 - 2h_4 + 2h_5 + 2h_6\right)$$

$$h_3^* = \frac{1}{2}\left(h_1 + 2h_4\right);\ \ h_4^* = \frac{1}{2}\left(h_1 + 2h_3\right) \qquad h_5^* = h_5; \qquad h_6^* = \frac{1}{2}\left(2h_1 + h_2\right) \tag{2.21}$$

(see Mishurova et al, 2016, for details)

Finally, one can write the following formulas for the effective elastic compliances of a short fiber reinforced composite (with orientation distribution of the fibers given by (2.13)) in the framework of non-interaction approximation:

$$s_1 = \frac{1-\nu_0}{4\mu_0(1+\nu_0)} + ch_1^*; \quad s_2 = \frac{1}{2\mu_0} + ch_2^*; \quad s_3 = \frac{-\nu_0}{2\mu_0(1+\nu_0)} + ch_3^*; \quad s_4 = s_3$$

$$s_5 = \frac{1}{\mu_0} + ch_5^*; \qquad s_6 = \frac{1}{2\mu_0(1+\nu_0)} + ch_6^* \tag{2.22}$$

where μ_0 and ν_0 are shear modulus and Poisson's ratio of the matrix.

Interaction between the inhomogeneities can be accounted for via deviation of the stress field acting on the inhomogeneities from remotely applied. In micromechanics, such a technique is called "effective field method". Below, we discuss two approaches to describe this deviation.

Mori-Tanaka-Benveniste scheme. This scheme, proposed by Mori and Tanaka (1973) and clarified by Benveniste (1987), assumes that each inhomogeneity, treated as isolated, is placed into a uniform field that is equal to its average over the matrix phase, and generally differs from the remotely applied one. The effective properties are calculated from the non-interaction approximation, by replacing the remotely applied field by the mentioned average one. The tensor of effective elastic compliances can be expressed in terms of the compliance contribution tensors $\boldsymbol{H}_i$ of inhomogeneities as follows (see, for example, Sevostianov and Kachanov, 2013):

$$\boldsymbol{S}^{eff} = \boldsymbol{S}^0 + \left[\frac{1}{V}\sum\nolimits_i V_i \boldsymbol{H}^i\right] : \left[\frac{1}{V}\sum\nolimits_i V_i \left(\boldsymbol{S}^i - \boldsymbol{S}^0\right)^{-1} : \boldsymbol{H}^i + (1-c)\boldsymbol{J}\right]^{-1} \tag{2.23}$$

Replacing the summation by averaging over orientations, in the case of the inhomogeneities of the same shape having the same elastic properties, yields

$$\boldsymbol{S}^{eff} = \boldsymbol{S}^0 + \left[\left(\boldsymbol{S}^1 - \boldsymbol{S}^0 \right)^{-1} + \frac{(1-c)}{c} \langle \boldsymbol{H} \rangle^{-1} \right]^{-1} \tag{2.24}$$

i.e. the effective elastic properties are expressed in terms of tensor $\langle \boldsymbol{H} \rangle$ given by (2.16)-(2.17).

Maxwell scheme. Maxwell homogenization scheme (Maxwell, 1873) can also be considered as a variant of the effective field method (Sevostianov and Kachanov, 2014). Sevostianov and Giraud (2013) and Sevostianov (2014) reformulated Maxwell's scheme for the general case of a composite with arbitrary orientation distribution of inhomogeneities of diverse shape using property contribution tensors. They suggested to cut the domain Ω of the volume V^* from a composite and place it into the matrix material. The effect produced by this element is described either by the sum of compliance contribution tensors of the inhomogeneities $\frac{1}{V}\sum_i V_i \boldsymbol{H}_i$ or by the compliance contribution tensor $\boldsymbol{H}_{eff}$ of the entire domain considered as an individual inhomogeneity with homogenized unknown properties. Equating these two quantities, the general equation for the Maxwell scheme can be obtained:

$$\frac{V^*}{V} \boldsymbol{H}_{eff} = \frac{1}{V} \sum_i V_i \boldsymbol{H}_i \tag{2.25}$$

The right hand side of the equation is known; the left hand side reflects the combined effect of overall properties of the material in Ω and its shape. According to (2.5), for an ellipsoidal shape of Ω, equation (2.19) yields

$$\boldsymbol{S}_{eff} = \boldsymbol{S}_0 + \left\{ \left[\frac{1}{V} \sum\nolimits_i V_i \boldsymbol{H}_{eff}^{\ i} \right]^{-1} - \boldsymbol{Q}_\Omega \right\}^{-1} \tag{2.26}$$

where $\boldsymbol{Q}_\Omega$ reflects effect of the shape of Ω and has to be calculated by (A.12). Replacing the summation by averaging over orientations yields

$$\boldsymbol{S}_{eff} = \boldsymbol{S}_0 + c \left\{ \langle \boldsymbol{H} \rangle^{-1} - c \boldsymbol{Q}_\Omega \right\}^{-1} \tag{2.27}$$

Thus, the effective elastic properties are again expressed in terms of tensor $\langle \boldsymbol{H} \rangle$.

The key parameter required for calculation of the components of this tensor is orientation scatter ζ entering (2.15) as the argument of functions $g_i(\zeta)$. This parameter can be evaluated experimentally using methods of computed X-ray tomography (CT). In the next section we show

the applicability of CT methodology for extraction of information on ODF on example of polymer fibers reinforced concrete.

3. Experimental.

Computed Tomography measures the linear absorption coefficient of the material in each point of the region of interest in the specimen. The coefficient is dependent on the incident X-ray energy and on the atomic number of the material. In most cases it can be regarded as linear, correlating to the specific density. In conventional systems, tomograms are measured slice by slice, and the sample is not only rotated, but also translated along a scan direction (Fig.5a). In more advanced types of tomography equipment, the object to be measured is moved constantly allowing the slices to generate a continuous volume. Measuring 2D slices allows using more efficient detectors and reduces stray radiation from the object.

In the case of 3D CT the detector no longer consists of a row of detectors but of a square field with an array of detector elements (Fig.5b). The detector measures conventional radiological images. Upon turning the object and acquiring a radiograph at each angle, a complete data set is collected within one turn. Computer programs are available to reconstruct the 3D volume from the radiographs. Resolutions in the micrometer range are achieved either by a high resolution detector (small pixel size, down to 0.2µm) and a parallel beam source (*e.g.*, with synchrotron radiation), or by an X-ray beam spot in the micro-meter range, and a coarse but efficient detector; in this case the cone beam geometry is exploited using a magnification set-up.

High penetration lengths can be achieved by higher accelerator voltages, which nowadays can reach 12MeV. This would lead to a maximal penetration length of 400mm, for materials as dense as iron, usable in CT reconstructions. The disadvantage is the minimum achievable spot size, which for high-energy devices is in the range of 1mm: the larger the spot size, the coarser the resolution. Standard X-ray tubes fill the gap between synchrotron sources and high-energy devices: they possess beam spots in the rage or a few micrometers, and have energies in the range of 100- 600 keV (accelerating voltages in kV).

In order to investigate highly absorbing materials, the choice of the highest possible X-ray energy is appropriate; however, it is important to limit both multiple scattering and transmission (an optimal transmission lies around 10-30%). Artefacts from beam hardening effects are reduced for high energies. In the case of two dimensional detectors, stray radiation may be

prevented by appropriate filters. To generate images from the measured data, mathematical processes like filtered back-projection, algebraic reconstruction, or iterative processes have to be used.

3.1. Specimens preparation.

Two sets of cement mortar prisms with size 40 x 40 x 160 mm have been produced (Fig 6a). The first set, consisting of Portland cement (CEM I 32.5 R), ground limestone, standard sand and water, was used as a reference. The specimens in second set contained polyacrylonitrile (PAC) fibers of diameter 15 µm and length 4 mm of various volume fractions. The preparation of mortar prisms was performed according to DIN EN 196-1. A conventional mortar mixer was used. After mixing, test specimens were compacted by using vibrating table and placed into a container with water for 24 hours. Then, all specimens were stored under water with temperature of 20°C.

Cylindrical specimens with length of 40 mm and diameter of 10 mm have been drilled from a mortar prism for CT measurements (Fig 6b). Before drilling, the prism was impregnated with epoxy resin in order to prevent disintegration of the sample. Fig 6c illustrates the geometry of the specimens relatively to the direction of mechanical tests.

3.2.Computed tomography.

The CT measurements were performed by using a CT scanner v|tome|x L 300 from General Electric. 3000 projection were acquired with acquisition time of 2s at voltage of 80 keV and tube current of 50µA. To obtain a better statistical sample of the orientation distribution of fibers within the sample, six CT measurements at different locations along the sample's height were carried out with spatial resolution of 6.65 µm. Examples of reconstructed slices of one of the 3D reconstructions are presented in Figure 7.

Image analysis of reconstructed volume was performed by using Amira ZIB Edition from Konrad-Zuse-Zentrum Berlin (ZIB). Due to the low contrast between the fibers and the matrix material, and because of the small fiber diameter (15 µm), identification of fibers by global segmentation was not possible. However, it was possible to trace fibers by using a template matching algorithm implemented in ZIB Amira. This tool creates correlation and orientation fields matching the reconstructed volume with a cylindrical template, which has to be defined by user. This approach helps to trace fibers (and others tube-like structure) even in noisy data. In the

present study, implementation of such algorithm had some limitations: Crossing of low-density fibers with pores and aggregates, as well as damage of fibers during sample drilling, resulted in difficulties in estimating fiber length. However, observations indicated that bending of fibers was not significant in this material. Therefore, reliable fiber orientation information could indeed be extracted even from incomplete or damaged fibers. The improper identification of material interface zones (such as the surface of aggregate particles) as fibers was minimized by introducing additional strategies, such as fiber length control and direction coefficient calculation.

As an output of the template matching algorithm, two orientation angles in spherical coordinates θ and φ for each fiber were obtained. Figure 8 presents examples of fiber orientation distributions in θ and φ obtained for one CT scan. These data were used to produce orientation distribution histograms (Fig. 9) normalized by the number of fibers for the whole sample. It is to be noted that in the concrete casting process polymer fibers are difficult to distribute with a defined orientation, due to the tendency of the fibers to agglomerate. From the orientation distribution histogram, a high number of fibers were oriented roughly parallel to the X-Z plane (θ near 0° or 180°) with orientation angle φ larger than 45° can be observed. To obtain the orientation distribution probability density, normalized frequency has to be multiplied by $52/\pi$ (since interval from 0 to $\pi/2$ is subdivided on 26 subintervals).

3.3.Reconstruction of the scatter parameter.

A custom Matlab script was developed to determine the scatter parameters ζ from CT data using nonlinear least squares fitting. The Trust Region Reflective method was used to minimize the squared second norm of the vector $\boldsymbol{e}$ denoting the error between the distribution (2.11) and the experimental data:

$$\min_{(\zeta)} \|\boldsymbol{e}\|_2^2 = \min_{(\zeta)} \left\| \frac{P(\varphi,\zeta)\sin\alpha - P_{exp}(\varphi)}{\overline{P}_{exp}(\varphi)} \right\|_2^2 \tag{3.1}$$

where $P(\varphi,\zeta)$ is the vector of probability density calculated using first of the expressions (2.11) for the given scatter parameter ζ and the inclination angle φ, $P_{exp}(\varphi)$ is the vector of experimentally obtained normalized frequencies and $\overline{P}_{exp}(\varphi)$ is the mean value of $P_{exp}(\varphi)$. Figure

10 a shows that the best fit is produced by $\zeta = 0$ with $R^2 = 0.9636$. It means that the distribution with respect to angle φ is isotropic and the material properties are transversely-isotropic with the isotropy plane x_2x_3 and symmetry axis x_1. We now change the coordinate system as shown in the inset of Figure 10b and recalculate the orientation distribution probability density with respect to angle $\tilde{\varphi}$ (Figure 10b). Again we use first of the expressions (2.11)and the best fit is produced by $\zeta = 3.8$ (red line in Figure 10b) with $R^2 = 0.9488$. Thus the overall distribution of the fibers is transversely-isotropic (at least, in the sense of approximate symmetry, Sevostianov and Kachanov, 2007) with x_1-axis being the axis of symmetry and with the scatter parameter $\zeta = 3.8$.

With the fitted fiber orientation distribution function, we can calculate the effective elastic properties of the composite. Figure 11 shows the effective engineering elastic constants calculated in the frameworks of NIA, Mori-Tanaka and Maxwell schemes for these orientation distribution. Material constants of the constituents are given in Table 1.

3.4.Mechanical tests.

For illustration, we also performed three points bending test (whose scheme is shown in Figure 6c) to evaluate the Young's modulus E_1 along x_1-axis. To estimate the elastic properties of the matrix, the same test was performed on unreinforced mortar (that did not contain any fibers). All specimens were tested on a Zwick rig Z050TN with test speed of 0.5 mm/min. Poisson's ratio of the mortar was measured independently and is 0.15. Young's modulus was calculated from the ratio of force F to maximal deflection w_{max} and geometrical parameters of the specimen as

$$E_1 = \frac{F}{w_{max}} \frac{L^3}{4a^4}, \tag{3.2}$$

where $L = 160mm$ is the specimen length and $a = 40mm$ is the side of the (square) cross-section. The circles in Figure 11b show the experimental data. We observe a very good agreement between the experimental data and the calculations. In spite of the fact that experimental data are only available for small volume fractions *c* of fibers, and in that interval of *c* all homogenization schemes yield similar results. In spite of the fact that we cannot prefer either of the homogenization schemes proposed above, the agreement between experiments and theory suggests that the model based on measured microstructural features is reliable.

4. Concluding remarks.

In order to calculate the equivalent elastic constants of a plastic fibers reinforced concrete composite (a transversely isotropic material), we considered the use of X-ray computed tomography to experimentally obtain information about orientation distribution of fibers. This experimental information was incorporated into several micromechanical homogenization schemes (non-interaction approximation, Mori-Tanaka-Benveniste, and Maxwell scheme). The results for one of the Young moduli were compared with experimental data obtained by three-point bending. They show very good agreement in the interval of moderate fiber volume fractions, and validate the approach set forth in this work.

Acknowledgement. This work was supported by National Group of Mathematical Physics GNFM-IndAM (Italy), FP7 Project TAMER IRSES-GA-2013-610547, NASA Cooperative Agreement NNX15AL51H (through NM Space Grant Consortium), and Bundesministerium für Bildung und Forschung (BMBF) grant 13N13306, and BAM Visiting Scientist Grant Program. The authors are grateful to Mr. Philipp Drabetzki (BAM, Berlin) for sample preparation.

References

Arenhart, R.G., Barra, G.M.O., and Fernandes, C.P. (2015) Simulation of percolation threshold and electrical conductivity in composites filled with conductive particles: effect of polydisperse particle size distribution. Polymer Composites, in press:12 August. doi:10.1002/pc.23155

Bay, R.S., Tucker, C.L. (1992) Stereological measurement and error estimates for three-dimensional fiber orientation. Polymer Engineering and Science, 32 (4), 240–253

Blanco, A. (2013) Characterization and modelling of SFRC elements. Doctoral Thesis. Barcelona: Universitat Politècnica de Catalunya.

Benveniste, Y. (1987). A new approach to the application of Mori-Tanaka's theory in composite material, Mechanics of Materials, 6, 147-157.

Bernasconi, A., Cosmi, F., Hine, P.J. (2012). Analysis of fibre orientation distribution in short fibre reinforced polymers: A comparison between optical and tomographic methods. Composites Science and Technology, 72, 2002–2008.

Bruno G., Fernandez Serrano R.- The dependence of the Eshelby model predictions on the microstructure of metal matrix composites Acta Materialia, Volume 55, Issue 4, February 2007, Pages 1267-1274

Chen, C. H. and Wang, Y.C. (1996). Effective thermal conductivity of misoriented shortfiber reinforced thermoplastics. Mechanics of Materials, 23(3), 217–228.

Chen, T., Dvorak G.J., Benveniste Y. (1992). Mori-Tanaka Estimates of the Overall Elastic Moduli of Certain Composite Materials. Journal of Applied Mechanics, 59(3), 539-546.

Chou, T.W. and Nomura, S. (1980-81). Fibre orientation effects on the thermoelastic properties of short-fiber composites, Fibre science & technology, 14, 279.

Clarke, A., Eberhardt, C. (1999). The representation of reinforcing fibres in composites as 3D space curves. Composites Science and Technology, 59, 1227–1237

DIN EN 196-1: Methods of testing cement – Part 1: Determination of strength.

Dunn, M.L., Ledbetter, H., Heyliger, P.L., Choi, C.S. (1996). Elastic constants of textured short-fiber composites. Journal of the Mechanics and Physics of Solids, 44, 1509-1541.

Dunn, M.L., Ledbetter H., (1997). Elastic–plastic behavior of textured short fiber composites, Acta Materialia, 45(8), 3327–3340.

Dunn, M.L., Ledbetter, H. (2000). Micromechanically-based acoustic characterization of the fiber orientation distribution function of morphologically textured short-fiber composites: prediction of thermomechanical and physical properties. Material Science and Engineering, A285, 56-61.

Duschlbauer, D., Bohm, H., and Pettermann, H. (2003). Numerical simulation of thermal conductivity of MMCs: Efect of thermal interface resistance. Materials Science & Technology, 19(8), 1107-1114.

Eberhardt, C., Clarke, A. (2001). Fibre-orientation measurements in short-glass-fibre composites. Part I: automated, high angular- resolution measurement by confocal microscopy, Composites Science and Technology, 61, 1389–1400.

Fernandez Serrano R., Bruno G., Gonzalez-Doncel G.- Correlation between residual stresses and the strength differential effect in PM 6061Al–15 vol% SiC_w composites: experiments,

models and predictions Acta Materialia, Volume 52, Issue 19, 8 November 2004, Pages 5471-5483Ferrari, M. (1991). Asymmetry and the high concentration limit of the Mori-Tanaka effective medium theory, Mechanics of Materials, 11 (3), 251-256.

Ferrari, M., Johnson, M.C. (1989) Effective elasticities of short-fiber composites with arbitrary orientation distribution, Mechanics of Materials, 8(1), 67-73.

Ferrari, M., Marzari, N. (1992). A Mori–Tanaka theory for textured short-fiber composites: application. Journal of Energy Resources Technology. 114(2), 101–104.

Fu, S.; Lauke, B. (1998). The elastic modulus of misaligned short-fiber-reinforced polymers. Composites Science and Technology, 58(3-4), 389–400.

Hashin, Z. (1983). Analysis of composite materials –a survey. Journal of Applied Mechanics, 50, 481–505.

Hill, R. (1965). A self-consistent mechanics of composite materials, Journal of the Mechanics and Physics of Solids, 13 (4), 213-222.

Horii, H. and Nemat-Nasser, S. (1983). Overall moduli of solids with microcracks: Load-induced anisotropy. Journal of the Mechanics and Physics of Solids, 31, 155–171.

Kachanov, M., Tsukrov, I., Shafiro, (1994) B. Effective Properties of Solids with Randomly Located Defects. Probabilities and Materials, ed. by D.Breusse, Kluwer Publ., 225-240.

Kachanov, M., and Sevostianov, I. (2005). On quantitative characterization of microstructures and effective properties. International Journal of Solids and Structures, 42, 309–336.

Kang, G., Yang, C., and Zhang, J. (2002) Tensile properties of randomly oriented short δ-Al2O3 fiber reinforced aluminum alloy composites. I. Microstructure characteristics, fracture mechanisms and strength prediction, Composites-A, 33, 647-656.

Kang, S. T., Lee, B. Y., Kimc, J.-K., Kim, Y. Y. (2011). The effect of fibre distribution characteristics on the flexural strength of steel fibre-reinforced ultra high strength concrete. Construction and Building Materials, 25(5), 2450–2457

Kang, S.-T., Kim, J.-K. (2012). Investigation on the flexural behavior of UHPCC considering the effect of fiber orientation distribution, Construction and Building Materials, 28, 57–65.

Kunin, I. A. (1983). Elastic media with microstructure. Berlin: Springer Verlag.

Lataste, J.F., Behloul, M., Breysse, D. (2008). Characterization of fibres distribution in a steel fibre reinforced concrete with electrical resistivity measurements. NDT and E International, 41(8), 638–47.

Lee, B. Y., Kim, J.-K., Kim, J.-S., Kim Y. Y. (2009). Quantitative evaluation technique of PVA (Polyvinyl Alcohol) fiber dispersion in engineered cementitious composites, Cement & Concrete Composites, 31(6), 408-417.

Li, S. (2000). General unit cells for micromechanical analyses of unidirectional composites. Composites Part A, 32, 815-826.

Liu, J., Li, C., Liu, J., Cui, G., Yang, Z. (2013). Study on 3D spatial distribution of steel fibers in fiber reinforced cementitious composites through micro-CT technique. Construction and Building Materials, 48, 656–661.

Lu, Y., Liaw, P.K. (1995). Effect of particle orientation in silicon-carbide particule-reiforced aluminium-matrix composite extrusions on ultrasonic velocity-measurements. Journal of composite materials, 29(8), 1096-1116

Maxwell, J. C. (1873). A treatise on electricity and magnetism. Oxford: Clarendon Press.

Mishurova, T., Cabeza, S., Bruno, G., Sevostianov, I. (2016). Average phase stress concentrations in multiphase metal matrix composites under compressive loading. International Journal of Engineering Science, 106, 245–261.

Mori, T., & Tanaka, K. (1973). Average stress in matrix and average elastic energy of materials with misfitting inclusions. Acta Metallurgica, 21, 571–574.

Nemat-Nasser, S., and Hori, M. (1993). Micromechanics: Overall properties of heterogeneous solids. Amsterdam: Elsevier.

Pérez, R., Banda, S., Ounaies, Z. (2008). Determination of the orientation distribution function in aligned single wall nanotube polymer nanocomposites by polarized Raman spectroscopy, Journal of Applied Physics, 103(7).

Pettermann, H. E., Bohm, H. J., and Rammerstorfer, F. G. (1997). Some direction dependent properties of matrix-inclusion type composites with given reinforcement orientation distributions, Composites Part B, 28B, 253-265.

Pujadas, P., Blanco, A., Cavalaro, S., de la Fuente, A., Aguado, A. (2014a) Multidirectional double punch test to assess the post-cracking behaviour and fibre orientation of FRC. Construction and Building Materials, 58, 214–224

Pujadas, P., Blanco, A., Cavalaro, S., de la Fuente, A., Aguado, A. (2014b). Fibre distribution in macro-plastic fibre reinforced concrete slab-panels. Construction and Building Materials, 64, 496–503

Redon, C., Chermant, L., Chermant, J.L., Coster, M. (1998). Assessment of fibre orientation in reinforced concrete, using Fourier image transform. Journal of Microscopy 191(3), 258-65.

Redon, C., Chermant, L., Chermant, J.L., Coster, M. (1999). Automatic image analysis and morphology of fibre reinforced concrete. Cement & Concrete Composites 21, 403-412.

Sevostianov, I. (2014). On the shape of effective inclusion in the Maxwell homogenization scheme for anisotropic elastic composites. Mechanics of Materials, 75, 45–59.

Sevostianov, I, and Giraud, A. (2013). Generalization of Maxwell homogenization scheme for elastic material containing inhomogeneities of diverse shape. International Journal of Engineering Science, 64, 23–36.

Sevostianov, I., and Kachanov, M. (1999). Compliance tensor of ellipsoidal inclusion. International Journal of Fracture, 96, L3–L7.

Sevostianov, I. and Kachanov, M. (2002) Elastic Compliances of Irregularly Shaped Cracks. International Journal of Fracture, 114, 245-257.

Sevostianov, I., and Kachanov, M. (2002). Explicit cross-property correlations for anisotropic two-phase composite materials. Journal of the Mechanics and Physics of Solids, 50, 253–282.

Sevostianov I. and Kachanov M. (2007). Relations between compliances of inhomogeneities having the same shape but different elastic constants. International Journal of Engineering Science, 45, 797–806.

Sevostianov, I. and Kachanov, M. (2013) Non-interaction approximation in the problem of effective properties. Chapter 1, Springer, 2013, 1-96.

Sevostianov, I. and Kachanov, M. (2014). On some controversial issues in theories of effective properties. Mechanics of Materials, 69, 93–105.

Sevostianov, I., Levin, V., Radi, E. (2016). Effective viscoelastic properties of short-fiber reinforced composites. International Journal of Engineering Science, 100, 61-73.

Suuronen, J.-P., Kallonen, A., Eik, M., Puttonen, J., Serimaa, R., Herrmann, H. (2013). Analysis of short fibres orientation in steel fibre-reinforced concrete (SFRC) by X-ray tomography, Journal of Material Science, 48, 1358–1367.

Takao, Y., Chou, T.W., Taya, M. (1982). Effective longitudinal young's modulus of misoriented short fiber composites. Journal of Applied Mechanics, 49, 536.

Tandon, G., Weng G.J. (1986). Average stress in the matrix and effective moduli of randomly oriented composites. Composites Science and Technology, 27(2), 111-132.

Tsuda, T., Ogasawara, T., Moon, S.-Y., Nakamotoc, K., Takedaa, N., Shimamurad, Y., Inoued Y. (2014). Three dimensional orientation angle distribution counting and calculation for the mechanical properties of aligned carbon nanotube/epoxy composites. Composites Part A: Applied Science and Manufacturing, 65, 1–9.

Turner, P.A., Signorelli, Bertinetti, J.W.M.A., and Bolmaro, R.E. (1999). Explicit method for calculating the effective properties and micromechanical stresses: an application to an alumina-SiC composite. Philosophical Magazine A, 79, 1379-1394

Walpole, L. J. (1966). On bounds for the overall elastic moduli of inhomogeneous systems. Journal of the Mechanics and Physics of Solids, 14, 151–162.

Walpole, L. J. (1984). Fourth-rank tensors of the thirty-two crystal classes: Multiplication tables. Proceedings of the Royal Society of London, A391, 149–179.

Zhu, Y.T., Blumenthal, W.R., Lowe, T.C. (1997). Determination of nonsymmetric 3-D fiber orientation distribution and average fiber length in short-fiber composites. Journal of Composite Materials, 31(13), 1287–1301.

Zhupanska, O. I. (2013). The Effect of Orientational Distribution of Nanotubes on Buckypaper Nanocomposite Mechanical Properties, Mechanics of Advanced Materials and Structures, 20(1).

Appendix. Tensor basis in the space of fourth rank tensors and representation of some tensors in its terms.

We outline a convenient technique of analytic inversion and multiplication of 4th rank tensors. It is based on expressing tensors in "standard" tensor bases as suggested by Kunin (1983) and Walpole (1984). In the case of the transversely isotropic elastic symmetry, the following basis is most convenient:

$$T^{(1)}_{ijkl} = \theta_{ij}\theta_{kl},\ T^{(2)}_{ijkl} = \left(\theta_{ik}\theta_{lj} + \theta_{il}\theta_{kj} - \theta_{ij}\theta_{kl}\right)/2,\ T^{(3)}_{ijkl} = \theta_{ij}m_k m_l,\ T^{(4)}_{ijkl} = m_i m_j \theta_{kl}$$

$$T^{(5)}_{ijkl} = \left(\theta_{ik}m_l m_j + \theta_{il}m_k m_j + \theta_{jk}m_l m_i + \theta_{jl}m_k m_i\right)/4,\ T^{(6)}_{ijkl} = m_i m_j m_k m_l \qquad \text{(A.1)}$$

where $\theta_{ij} = \delta_{ij} - m_i m_j$ and $\boldsymbol{m} = m_1\boldsymbol{e}_1 + m_2\boldsymbol{e}_2 + m_3\boldsymbol{e}_3$ is a unit vector along the axis of transverse symmetry.

These tensors form the closed algebra with respect to the operation of (non-commutative) multiplication (contraction over two indices):

$$\left(\boldsymbol{T}^{(\alpha)} : \boldsymbol{T}^{(\beta)}\right)_{ijkl} \equiv T^{(\alpha)}_{ijpq}T^{(\beta)}_{pqkl} \qquad \text{(A.2)}$$

The inverse of any fourth rank tensor $\boldsymbol{X}$, as well as the product $\boldsymbol{X}:\boldsymbol{Y}$ of two such tensors are readily found in the closed form, as soon as the representations in the basis

$$\boldsymbol{X} = \sum_{k=1}^{6} X_k \boldsymbol{T}^{(k)},\ \boldsymbol{Y} = \sum_{k=1}^{6} Y_k \boldsymbol{T}^{(k)} \qquad \text{(A.3)}$$

are established. Indeed:

a) inverse tensor $\boldsymbol{X}^{-1}$ defined by $X^{-1}_{ijmn}X_{mnkl} = \left(X_{ijmn}X^{-1}_{mnkl}\right) = J_{ijkl}$ is given by

$$\boldsymbol{X}^{-1} = \frac{X_6}{2\Delta}\boldsymbol{T}^{(1)} + \frac{1}{X_2}\boldsymbol{T}^{(2)} - \frac{X_3}{\Delta}\boldsymbol{T}^{(3)} - \frac{X_4}{\Delta}\boldsymbol{T}^{(4)} + \frac{4}{X_5}\boldsymbol{T}^{(5)} + \frac{2X_1}{\Delta}\boldsymbol{T}^{(6)} \qquad \text{(A.4)}$$

where $\Delta = 2\left(X_1X_6 - X_3X_4\right)$.

b) product of two tensors $\boldsymbol{X}:\boldsymbol{Y}$ (tensor with $ijkl$ components equal to $X_{ijmn}Y_{mnkl}$) is

$$\begin{aligned}\boldsymbol{X}:\boldsymbol{Y} = {} & \left(2X_1Y_1 + X_3Y_4\right)\boldsymbol{T}^{(1)} + X_2Y_2\boldsymbol{T}^{(2)} + \left(2X_1Y_3 + X_3Y_6\right)\boldsymbol{T}^{(3)} \\ & + \left(2X_4Y_1 + X_6Y_4\right)\boldsymbol{T}^{(4)} + \frac{1}{2}X_5Y_5\boldsymbol{T}^{(5)} + \left(X_6Y_6 + 2X_4Y_3\right)\boldsymbol{T}^{(6)}\end{aligned} \qquad \text{(A.5)}$$

If x_3 is the axis of transverse symmetry, the general transversely isotropic fourth-rank tensor, being represented in this basis

$$\Psi_{ijkl} = \sum \psi_m T^m_{ijkl} \tag{A.6}$$

has the following components:

$$\psi_1 = (\Psi_{1111} + \Psi_{1122})/2;\ \psi_2 = 2\Psi_{1212};\ \psi_3 = \Psi_{1133};\ \psi_4 = \Psi_{3311};\tag{A.7}$$

$$\psi_5 = 4\Psi_{1313};\ \psi_6 = \Psi_{3333}$$

Utilizing (A.7) one obtains the following representations:

• The tensor of elastic compliances of an isotropic material $S_{ijkl} = \sum s_m T^m_{ijkl}$ has the following components

$$s_1 = \frac{1-\nu}{4\mu(1+\nu)};\ s_2 = \frac{1}{2\mu};\ s_3 = s_4 = \frac{-\nu}{2\mu(1+\nu)};\ s_5 = \frac{1}{\mu};\ s_6 = \frac{1}{2\mu(1+\nu)}. \tag{A.8}$$

• The tensor of elastic stiffness of an isotropic material by $C_{ijkl} = \sum c_m T^m_{ijkl}$ has components

$$c_1 = \lambda + \mu;\ c_2 = 2\mu;\ c_3 = c_4 = \lambda;\ c_5 = 4\mu;\ c_6 = \lambda + 2\mu. \tag{A.9}$$

where $\lambda = 2\mu\nu/(1-2\nu)$.

• Unit fourth rank tensors are represented in the form

$$J^{(1)}_{ijkl} = \left(\delta_{ik}\delta_{lj} + \delta_{il}\delta_{kj}\right)/2 = \frac{1}{2}T^1_{ijkl} + T^2_{ijkl} + 2T^5_{ijkl} + T^6_{ijkl} \tag{A.10}$$

$$J^{(2)}_{ijkl} = \delta_{ij}\delta_{kl} = T^1_{ijkl} + T^3_{ijkl} + T^4_{ijkl} + T^6_{ijkl} \tag{A.11}$$

• Tensor $\boldsymbol{Q}$ defined by (2.6) , in the case of a spheroidal inhomogeneity ($a_1 = a_2 = a$) of the aspect ratio $\gamma = a/a_3$, has the following components (see, for example, Sevostianov and Kachanov, 2002):

$$q_1 = \mu[4\kappa - 1 - 2(3\kappa - 1)f_0 - 2\kappa f_1], \qquad q_2 = 2\mu[1 - (2-\kappa)f_0 - \kappa f_1]$$

$$q_3 = q_4 = 2\mu[(2\kappa - 1)f_0 + 2\kappa f_1], \qquad q_5 = 4\mu(f_0 + 4\kappa f_1), \quad q_6 = 8\mu(\kappa f_0 - \kappa f_1) \tag{A.12}$$

where $\kappa = 1/[2(1-\nu)]$ and functions f_0 and f_1 are given by

$$f_0 = \frac{1-g}{2(1-\gamma^2)}, \quad f_1 = \frac{1}{4(1-\gamma^2)^2}\left[\left(2+\gamma^2\right)g - 3\gamma^2\right] \tag{A.13}$$

where

$$g(\gamma)=\begin{cases}\dfrac{\gamma^2}{\sqrt{\gamma^2-1}}arctan\sqrt{\gamma^2-1}, & oblate\,spheroid, \gamma \geq 1 \\ \dfrac{\gamma^2}{2\sqrt{1-\gamma^2}}ln\dfrac{1+\sqrt{1-\gamma^2}}{1-\sqrt{1-\gamma^2}}, & prolate\,spheroid, \gamma \leq 1\end{cases} \tag{A.14}$$

Factors entering the representation of the compliance contribution tensor $\boldsymbol{H}$ of the spheroidal inhomogeneity with bulk and shear moduli K_1 and μ_1 embedded in the matrix with elastic constants K_0 and μ_0 in terms of the tensor basis are given by (Sevostianov and Kachanov, 1999; 2002):

$$h_1 = \frac{1}{2\Delta}\left[K + \frac{4}{3}\mu + q_6\right];\ h_2 = \frac{1}{2\mu + q_2};\ h_5 = \frac{4}{4\mu + q_5}$$

$$h_3 = h_4 = -\frac{1}{\Delta}\left[K - \frac{2}{3}\mu + q_3\right];\ h_6 = \frac{2}{\Delta}\left[K + \frac{1}{3}\mu + q_1\right] \tag{A.15}$$

where K and μ are defined by (2.15) and

$$\Delta_H = 2\left[3\mu K + K(q_1 + q_6 - 2q_3) + \frac{\mu}{3}(4q_1 + q_6 + 4q_3) + \left(q_1 q_6 - q_3^2\right)\right] \tag{A.16}$$

Tables.

Table 1. Mechanical properties of the constituents

	Young's modulus (GPa)	**Poisson's ratio**
Concrete matrix	45.0	0.15
Polyacrylonitrile fibers	26.8	0.19

Figure captions

Figure 1. Optical micrographs showing orientation distribution of fibers: (a) -Al2O3 fibers reinforced aluminum alloy (from Kang et al, 2002); (b) polypyrrole-coated amorphous silica short fibers reinforced polyvinylidene fluoride matrix (from Arenhart et al, 2015).

Figure 2. Spherical coordinate system used in (2.9).

Figure 3. (a) Dependence of the orientation distribution function P_ζ defined by the first equation (2.11) on angle φ at several values of ζ; (b) dependence of $P_\zeta \sin\varphi$ on angle φ; (c) dependence of the orientation distribution function P_ζ defined by the second equation (2.11) on angle θ.

Figure 4. Dependence of functions $g_i(\zeta)$ on the scatter parameter.

Figure 5. Schematic diagram of the computed tomography: (a) conventional system - tomograms are measured slice by slice, and the sample is not only rotated, but also translated along a scan direction; (b) 3D CT - the detector no longer consists of a row of detectors but of a square field with an array of detector elements

Figure 6. (a) concrete specimens used in mechanical tests; (b) specimens used for computed tomography experiments; (c) schematic representation of samples used for mechanical testing and CT.

Figure 7. 2D reconstructed slices from CT measurements (a) in plane x_1x_3 and (b) in plane x_2x_3.

Figure 8. Depiction of fiber orientation distribution obtained by CT measurements with respect to angles φ (a) and θ (b).

Figure 9. Histograms of normalized frequency distribution for angles φ (a) and θ (b).

Figure 10. (a) Orientation distribution function for angle φ and its best fit by the first equation (2.11); (b) orientation distribution function for angle $\tilde{\varphi}$ in the coordinate system shown in the inset and its best fit by the first equation (2.11).

Figure 11. Dependence of the elastic constants (in GPa) of the PAC fibers reinforced concrete on the volume fraction of fibers. Calculations are done according to formulas (2.22) (non-interaction approximation), (2.24) (Mori-Tanaka-Benveniste scheme), and (2.27) (Maxwell scheme). Figure (b) provides comparison with the experimental data indicated by circles.

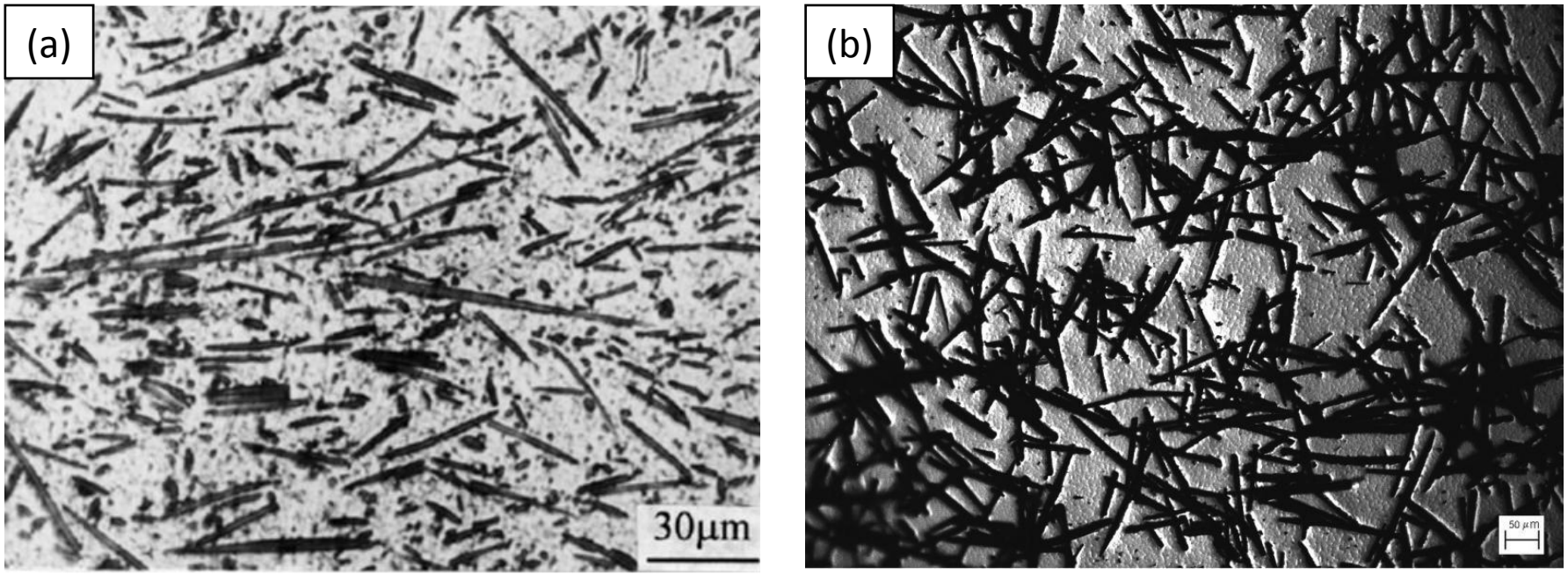

Figure 1

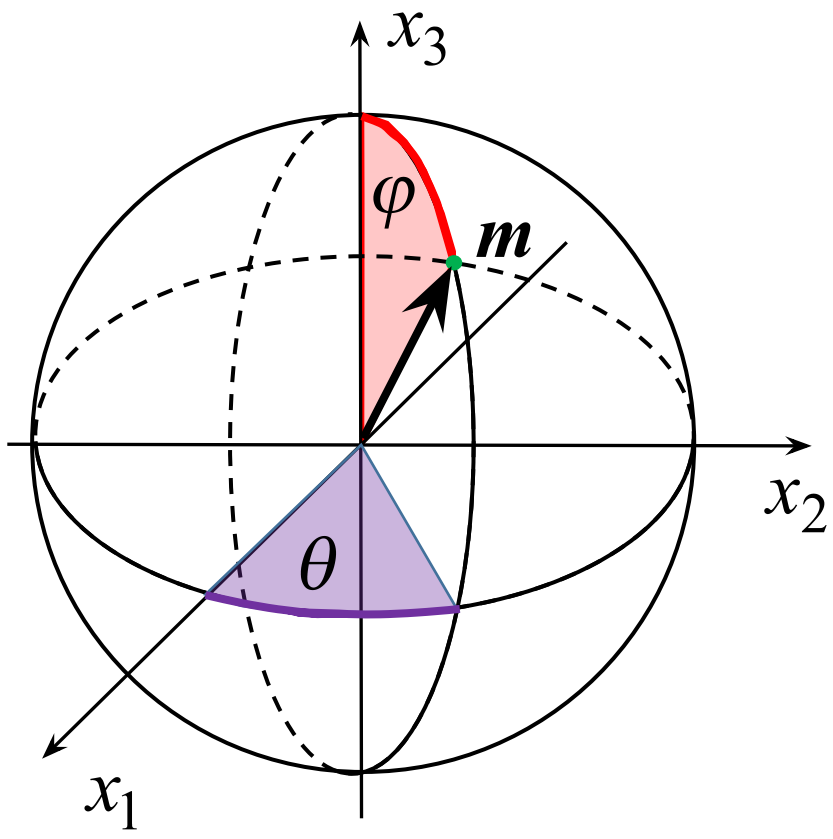

Figure 2

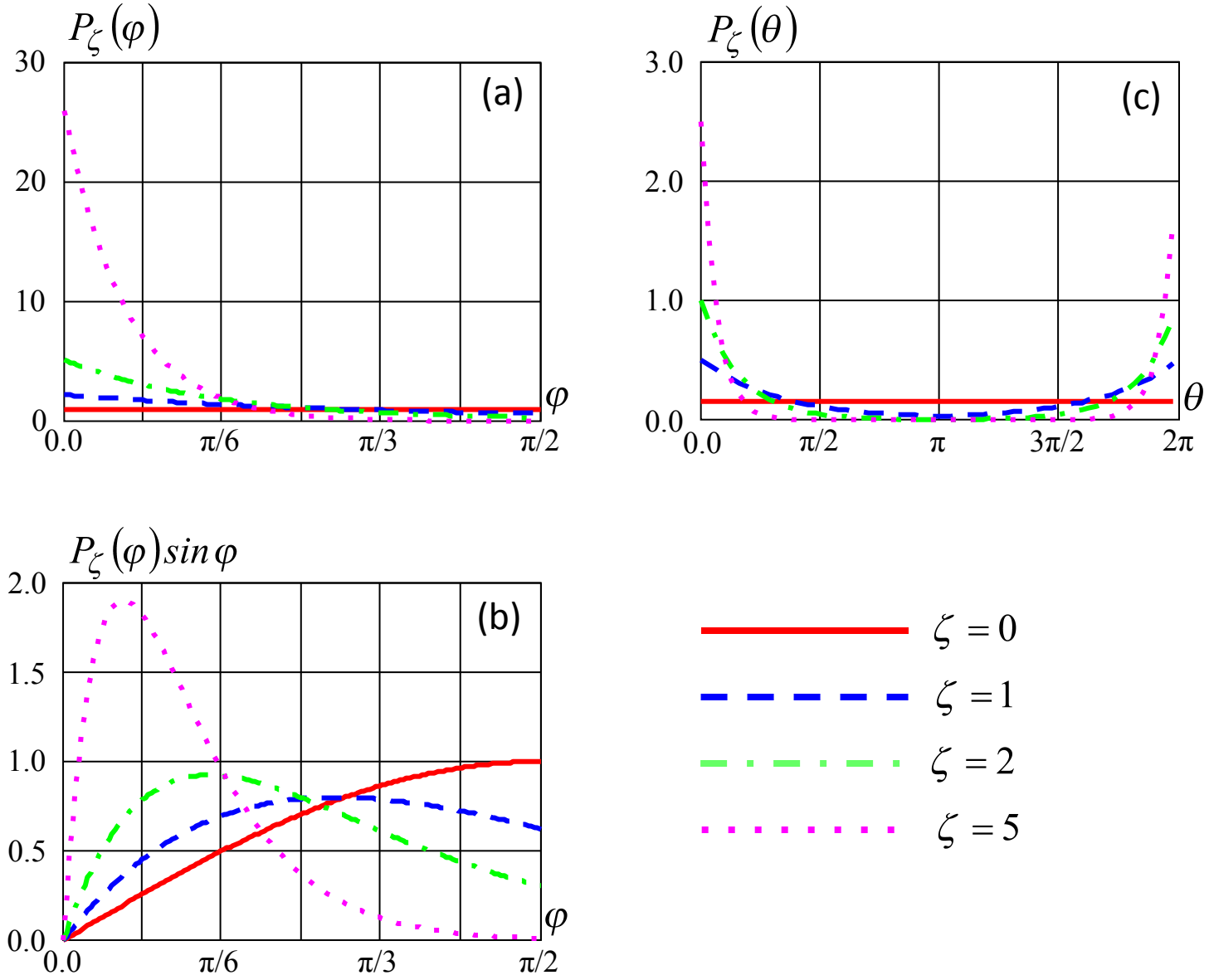
$P_\zeta(\varphi)$
30
20
10
0
(a)
φ
0.0
π/6
π/3
π/2
$P_\zeta(\theta)$
3.0
2.0
1.0
0.0
(c)
θ
0.0
π/2
π
3π/2
2π
$P_\zeta(\varphi)\sin\varphi$
2.0
1.5
1.0
0.5
0.0
(b)
φ
0.0
π/6
π/3
π/2
$\zeta = 0$
$\zeta = 1$
$\zeta = 2$
$\zeta = 5$

Figure 3

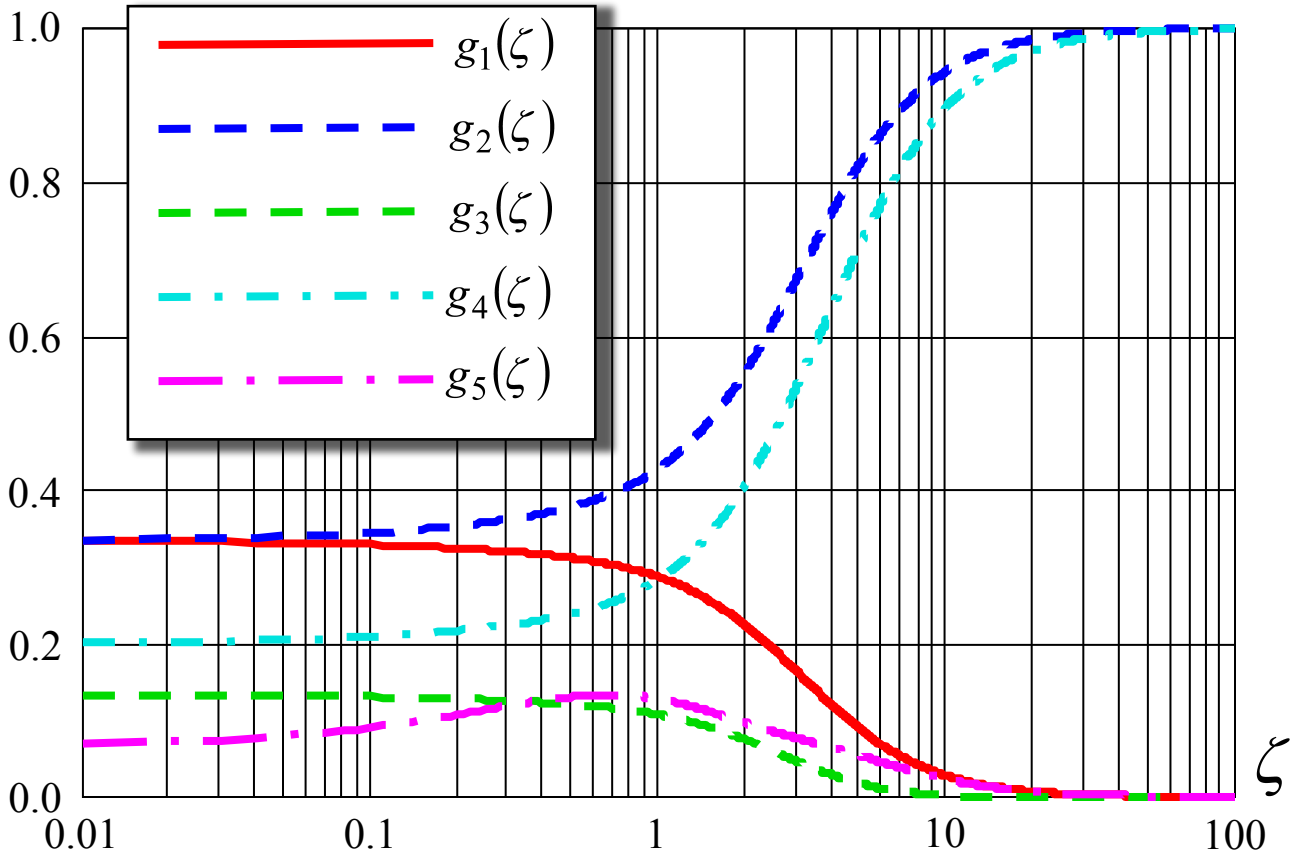
1.0
0.8
0.6
0.4
0.2
0.0
0.01
0.1
1
10
100
ζ
$g_1(\zeta)$
$g_2(\zeta)$
$g_3(\zeta)$
$g_4(\zeta)$
$g_5(\zeta)$

Figure 4

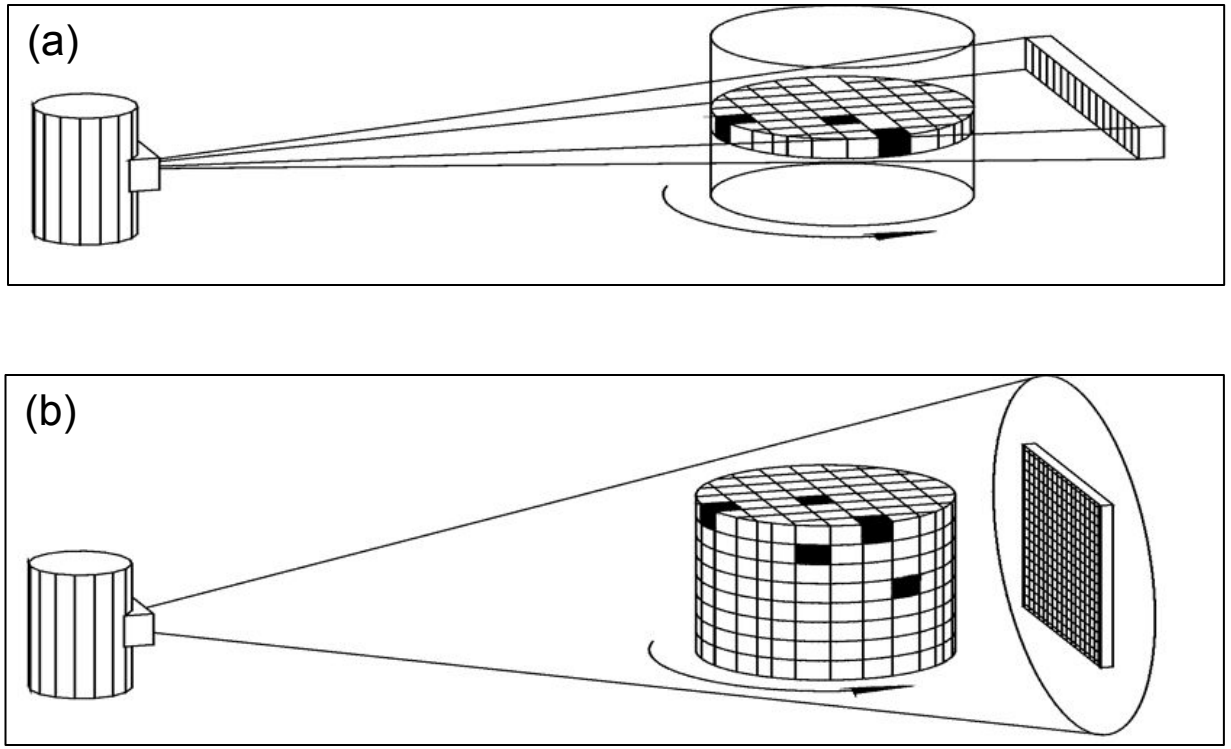

Figure 5

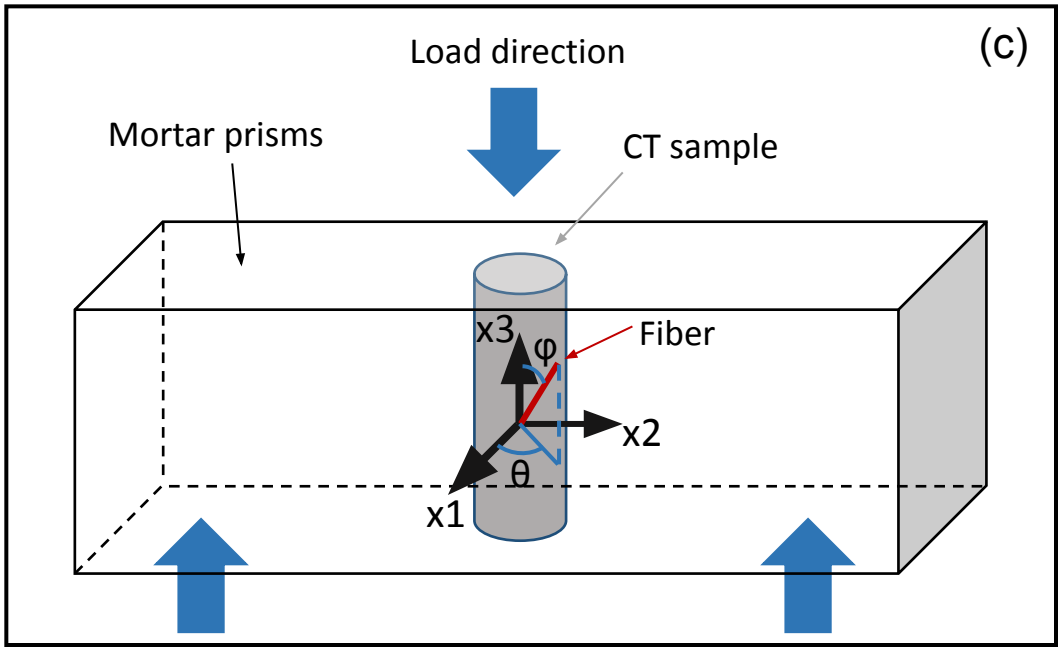

Figure 6

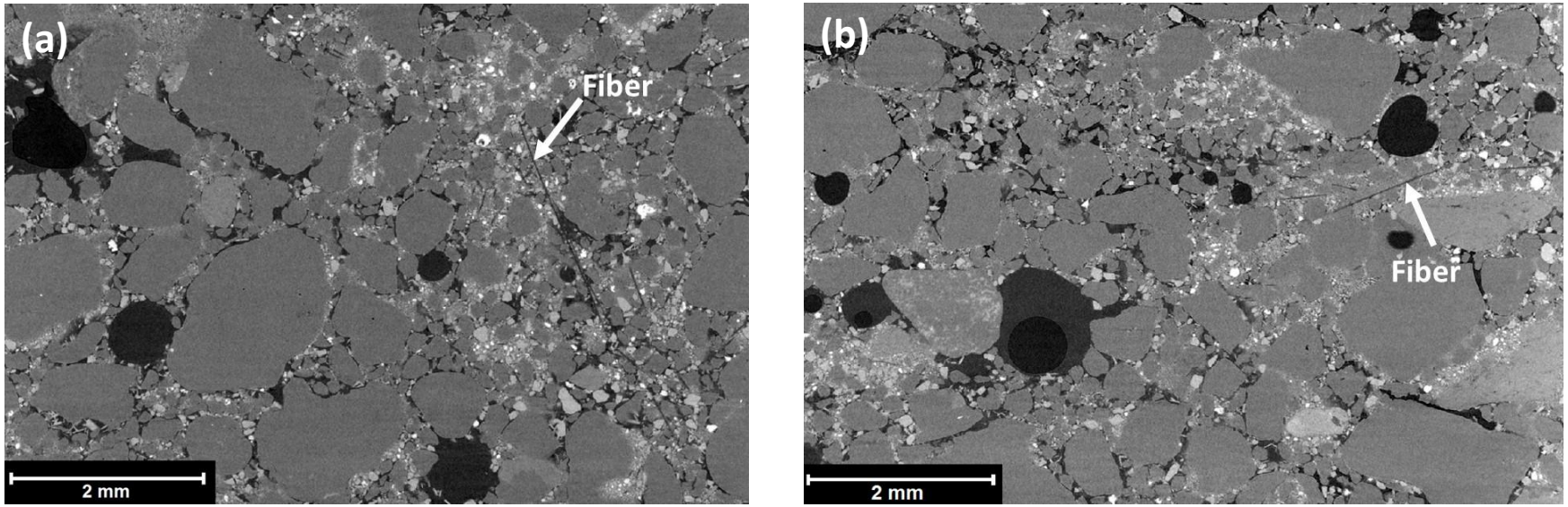

2D reconstructed slices from CT measurements (a) in plane X1X3 and (b) in plane X2X3

Figure 7

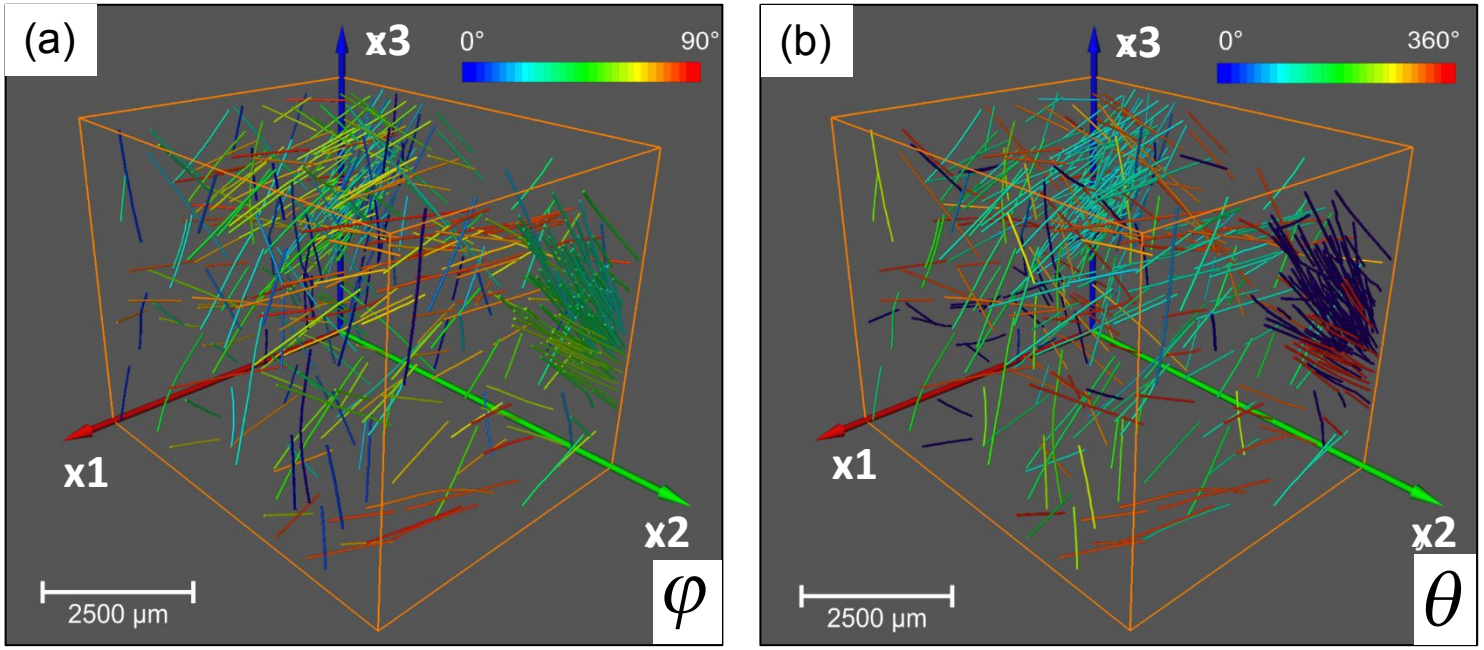

Figure 8

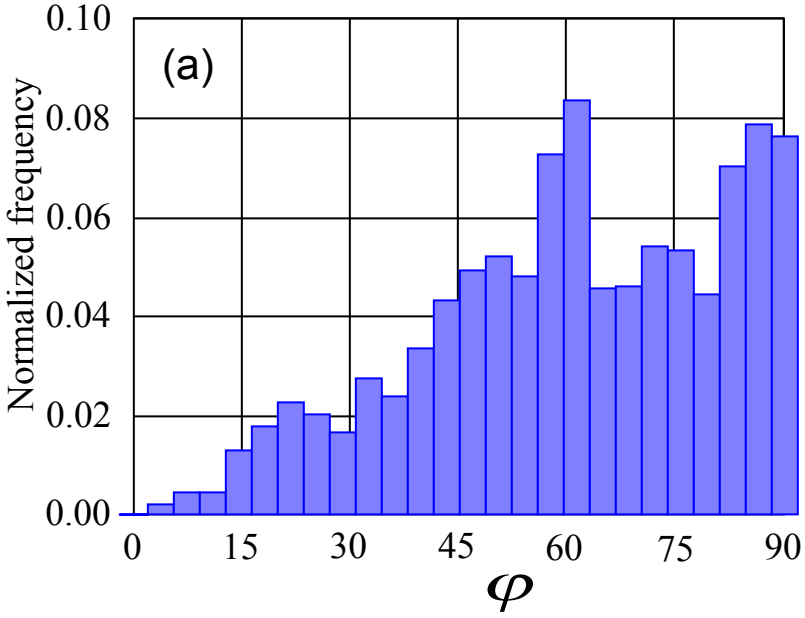
(a)
Normalized frequency
0.10
0.08
0.06
0.04
0.02
0.00
0
15
30
45
60
75
90
φ

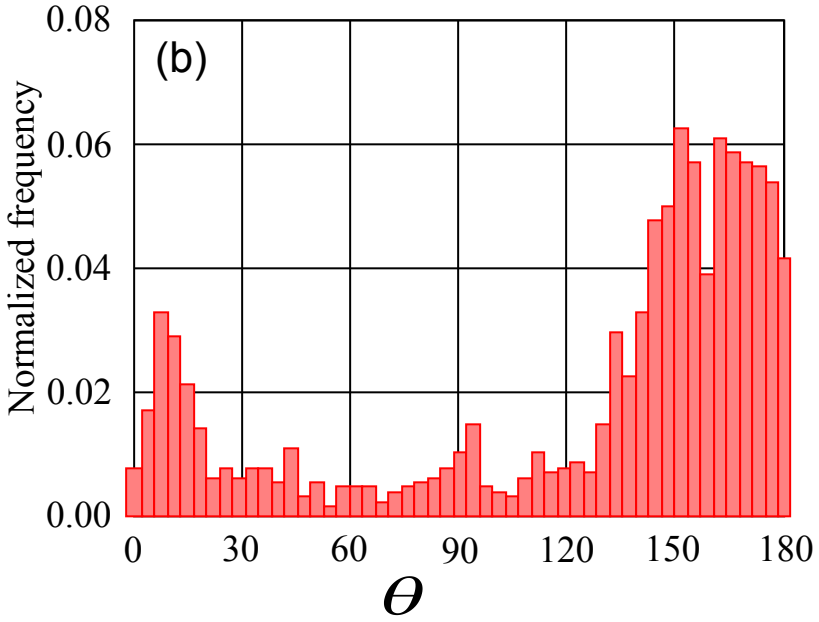
(b)
Normalized frequency
0.08
0.06
0.04
0.02
0.00
0
30
60
90
120
150
180
θ

Figure 9

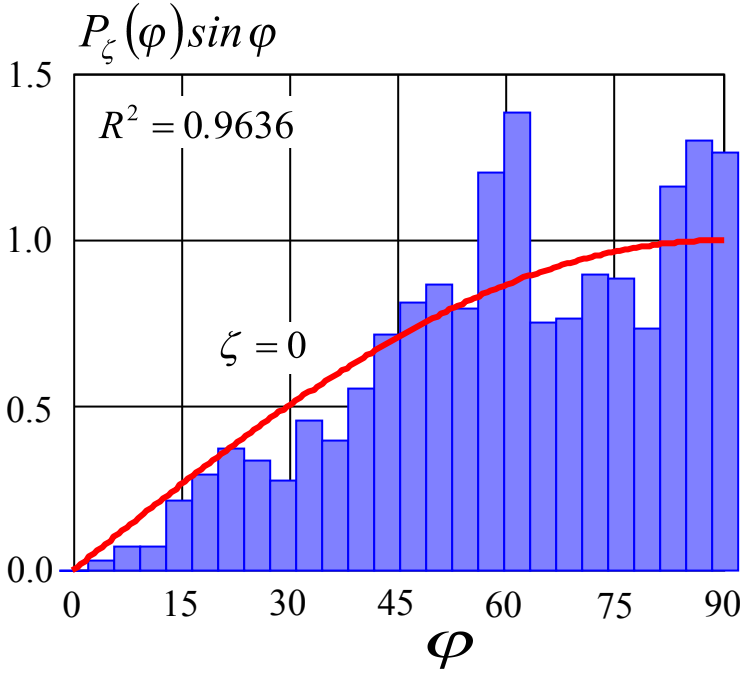
$P_\zeta(\varphi)\sin\varphi$
$R^2 = 0.9636$
$\zeta = 0$
1.5
1.0
0.5
0.0
0
15
30
45
60
75
90
φ

(a)

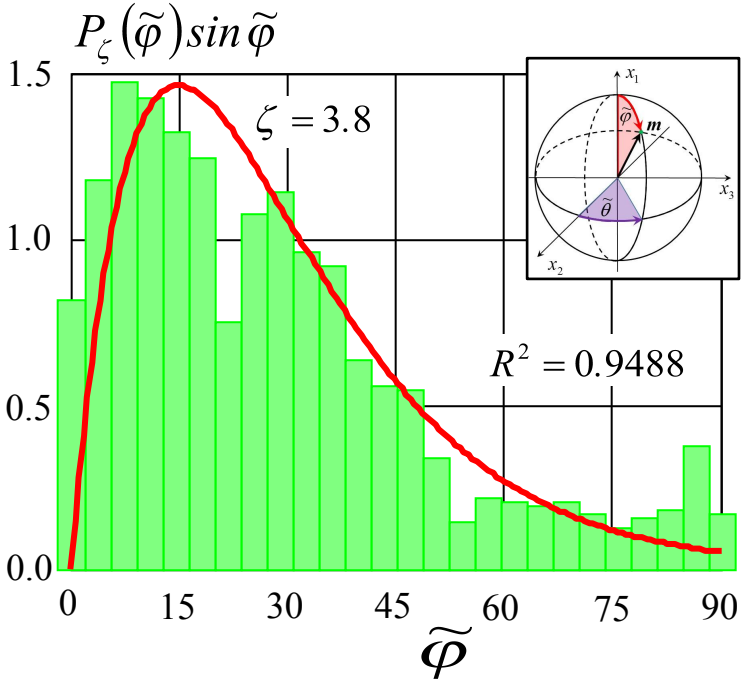
$P_\zeta(\tilde{\varphi})\sin\tilde{\varphi}$
$\zeta = 3.8$
$R^2 = 0.9488$
1.5
1.0
0.5
0.0
0
15
30
45
60
75
90
$\tilde{\varphi}$
x_1
x_2
x_3
$\tilde{\varphi}$
m
$\tilde{\theta}$

(b)

Figure 10

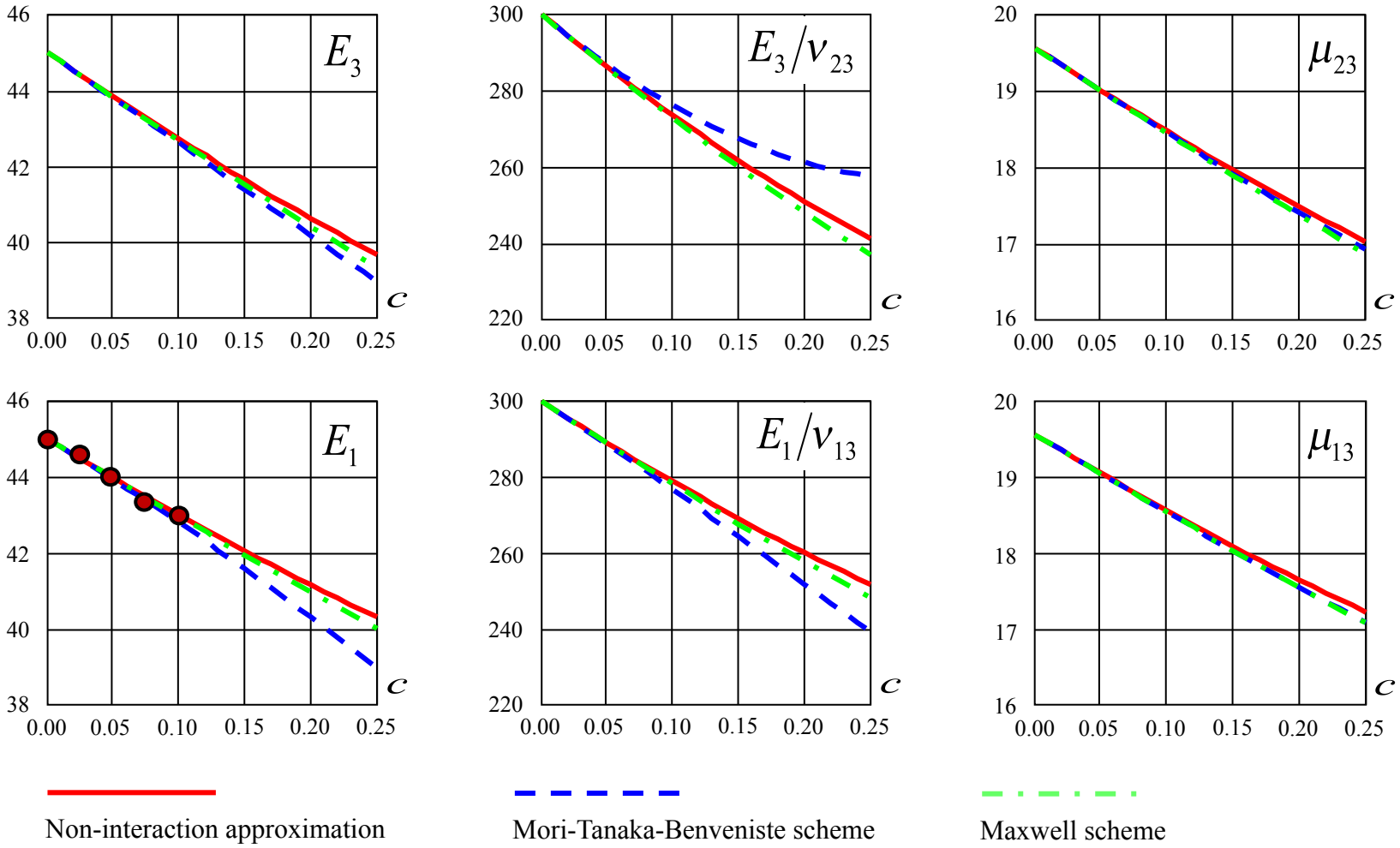
E_3
E_3/ν_{23}
μ_{23}
E_1
E_1/ν_{13}
μ_{13}
c
Non-interaction approximation
Mori-Tanaka-Benveniste scheme
Maxwell scheme

Figure 11